Numerical Simulation of Missile Jet Deflector

Souraseni Basu,* Soumyajit Saha,* and Debasis Chakraborty†

Defence Research and Development Laboratory, Hyderabad 500 058, India

A numerical simulation was carried out to estimate the heat flux on a jet deflector caused due to impingement of the rocket exhaust of a canisterized missile. Three-dimensional Navier–Stokes equations were solved along with shear-stress transport k-ω turbulence model using commercial computational fluid dynamics software. The firings of a short-burn rocket motor as well as a full-burn rocket motor with a jet vane are simulated. Jet vanes are found to have significant influence in the plume spreading and impinging heat flux rate. The measured erosion patterns of both the rocket motors are seen to scale with the computed heat flux. In spite of the different jet characteristics of the two motors, it is observed that the erosion rate per megawatt per square meter heat flux rate is not very different. It is demonstrated that erosion of the composite liner due to jet impingement is mostly dependent on the heat flux on the deflector surface.

I. Introduction

VERTICAL launching is the preferred choice of surface to air missiles from a mobile ground system. The exhaust jet from a rocket motor is diverted by an inclined plate away from the launcher, as shown in Fig. 1. The study of supersonic jets impinging on an inclined flat plate is important for scientific investigation as well as practical applications. Apart from the design of a jet deflector, the jet impingement problem in inclined plates appears in the design of multistage rocket separation at a higher-attitude rocket test-stand environment, plume ducting system of canisterized missiles, space module attitude-control thrusters operation, etc. Many complex fluid dynamics phenomena like shock/shock interactions and shock/boundary-layer interactions exist in such flowfields. Design parameters like the inclined angle of the plate, jet pressure ratios, and the nozzle-plate distance greatly affect the structure of such flowfields. Inclined jet impingement exhibits more complex features than the perpendicular jet impingement [1,2]. Because of complex shock/shock interactions, the maximum pressure on the inclined plate can be significantly larger than that on the perpendicular plate. Indeed, it is a great challenge to understand the physics of these flows and correctly predict the heat and pressure loads on the impinging plate.

Lamont and Hunt [3] carried out experimental investigations of supersonic jet impingement on an inclined plate through pressure measurements and shadowgraph visualizations, and they demonstrated that the plate inclination has a strong influence on the pressure distribution. Nakai et al. [4,5] investigated supersonic jet impingement on an inclined plate with different inclination angles, pressure ratios, and nozzle-plate distances with pressure-sensitive paints for surface pressure measurements and schlieren photography for flow visualization. According to Edney's [6] classification of shock/shock interactions (depending upon how impinging shocks interact with the bow shock), type 1 shock/shock interaction is mostly observed when the plate is nearly perpendicular to the jet, the nozzle-plate distance is large, and the pressure ratio is low. For a plate angle θ of less than 50 deg, a type 2 flowfield occurs; for $\theta < 30$ deg, the intermediate tail shock wave merges with the barrel shock wave and gives rise to a type 3 flowfield. Earlier, analytical expression and semiempirical correlations [7,8] were used to predict the plume impingement forces and heat load. However, the correlations were

limited to the particular model test conditions, and they could not be generally applied. Moreover, they did not correctly predict the surface pressure distribution but gave only the correct order of magnitude of the pressure peak. The number of numerical simulations, including Reynolds-averaged Navier–Stokes (RANS) [9,10], large-eddy simulation [11] and Weighted Essentially NonOscillatory (WENO) schemey [12], described various features of this complex fluid dynamic problem. Dharavath and Chakraborty [10] demonstrated that well-resolved RANS simulations with the standard k-ε turbulence model were able to predict the experimental pressures and other finer details of supersonic impinging jets on an inclined plate.

To protect the deflector assembly from the hot jet, the surface of the deflector is coated with a heat-resistant liner. The liner is required to withstand the worst-case scenario of the hang fire of a missile on a launcher, as well as to protect the deflector. Estimation of the erosion of the liner due to hot impingement of the exhaust gas is of paramount importance to the designer. The overall process of thermochemical ablation is extremely complex, with the interplay of numerous factors, including the solid-propellant composition, motor operating conditions, duration of firing, nozzle geometry, material properties of the liner, rates of species diffusion, surface and gas phase chemical reactions, etc. Analytical/semiempirical models [13–16] for prediction of the thermal response of the materials undergoing decomposition are very much configuration dependent. Henderson and Wieck [14] reviewed different semiempirical and analytical models for thermochemical ablation. Ogasawara et al. [17] conducted an experimental investigation in an arcjet facility with a supersonic plasma airstream to determine the thermal performance and erosive characteristics of a carbon composite with a silicon based polymer. Siddiqui and Balasubrahmanyam [18] developed a one-dimensional transient thermal model to predict the erosion of charring and noncharring ablative liners. The model was able to predict the experimental observations of carbon-phenolic and graphite liners. Bianchi et al. [19] presented a thermochemical erosion analysis for graphite/carbon–carbon rocket nozzle considering the solution of the RANS equation in the nozzle, the heterogeneous chemical reaction at the nozzle surface, and heat conduction in the nozzle material. The results indicated that the erosion rate was diffusion limited for a metalized propellant and kinetic limited for a nonmetallized propellant. It is clear from the preceding discussion that erosion characterization of a polymeric liner under severe mechanical and thermal loads requires further study.

In the present work, a numerical simulation is performed to estimate the heat flux of a jet deflector caused due to hot impingement of the rocket exhaust of a canisterized missile. Three-dimensional Navier–Stokes equations are solved with the shear-stress transport (SST) k-ω turbulence model using the commercial computational fluid dynamics (CFD) software FLUENT [20]. The erosion pattern found in a short-duration rocket motor test was found to be similar to the computed heat flux distribution, and the measured erosion data

*Directorate of Computational Dynamics, Kanchanbagh.
†Directorate of Computational Dynamics, Kanchanbagh; debasis_cfd@drdl.drdo.in.

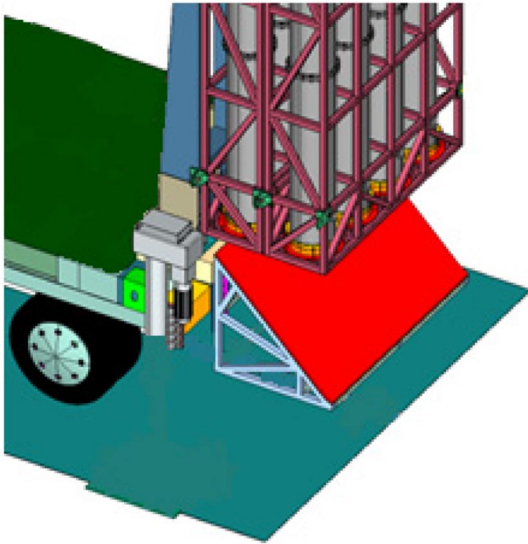Fig. 1   Jet deflector of the mobile launcher.

Fig. 3   Computational (hexahedral) grid in the flow domain.

were correlated with a CFD simulated cold-wall heat flux. The liner erosion for the full-duration test was predicted from the computed cold-wall heat flux, and a close match was observed between the test data and the prediction.

II.   Simulation of Short-Duration Motor

A.   Simulation Domain, Solution Methodology, and Boundary Conditions

The cold-wall heat flux on a jet deflector for a short-duration motor was estimated numerically. The stagnation pressure, stagnation temperature, and mass flow rate of the rocket motor were 31 bar, 3140 K, and 3.41 kg/s, respectively. The motor did not have any jet vane thrust vector control (TVC). The schematic of the computational domain, as viewed from the side of the deflector, is shown in Fig. 2. (All linear dimensions are nondimensionalized with the rocket motor exit diameter D.) The computational domain was taken as sufficiently large to minimize the effect of the jet flow affecting the ambient inlet/outlet boundary conditions. The left-side inlet plane was at a distance $4.2D$ from the deflector plate, and the right-side outlet plane was at a distance $30D$ from the left inlet plane. The distance from the top plane to the bottom wall plane was $18D$. The motor inlet was prescribed a pressure of 31 bar and a temperature of 3140 K, whereas the atmospheric conditions (1 bar of pressure and 300 K temperature) were prescribed in the top and side planes. To allow the entrainment of air, ambient pressure was prescribed in the gap between the side motion arrestor plate and the missile. The missile was coaxial with a cylindrical canister. There was an annular
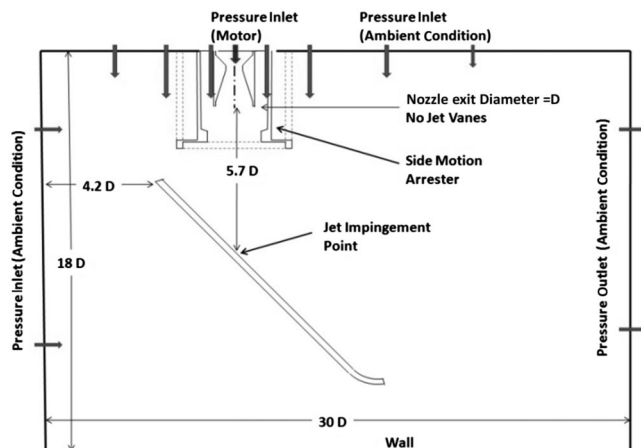
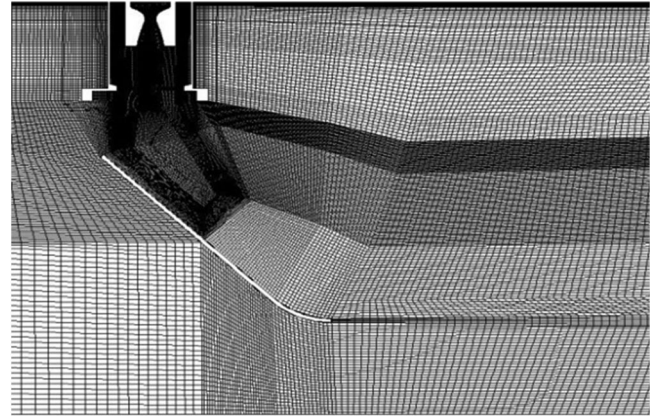gap between the canister and the missile that allowed entrainment of the cold ambient air due to the effect of plume flow through the motor inlet. The circular canister was supported on a square supporting base attached to the structure of the launcher. The domain was discretized using around 4.3 million hexahedral grid nodes, using the commercial grid generator ICEM CFD [21], shown in Fig. 3. The first cell height on the deflector surface was about 5 μm, which was sufficient enough to obtain a y^+ value close to one, at the jet impingement point, for proper estimation of the heat flux. Unsteady three-dimensional (3-D) Reynolds-averaged unsteady Navier–Stokes equations were solved with the SST k-ω turbulence model. A density-based solver with the second-order spatially accurate Roe/flux difference splitting scheme [22] and the second-order-accurate temporal discretization is used. The rocket exhaust plume was considered a separate species, and the governing equation for species transport was solved to simulate mixing of the plume with air. The top surface of the deflector was given an isothermal 300 K temperature for the estimation of the cold-wall heat flux. Ambient pressure (1 bar) was specified at the external boundaries.

B.   Results and Discussions

Simulations were carried out until the mean heat flux at the jet impingement point on the deflector surface became constant. The residues obtained were on the order of 10^{-3}. To study the grid convergence of the results, simulations were carried out for two grids with sizes of 4.3 and 6.6 million. The zones where significant flow gradient exists, the grid are finer. For example, in the shear layer between the hot exhaust and the ambient air, the grid spacing is 5 mm for the finer grid as compared to 8 mm spacing for the coarser grid. The average convective heat flux distributions with these two grids are compared in Fig. 4. The results are shown to agree very well, demonstrating the grid independence of the results. Temporal

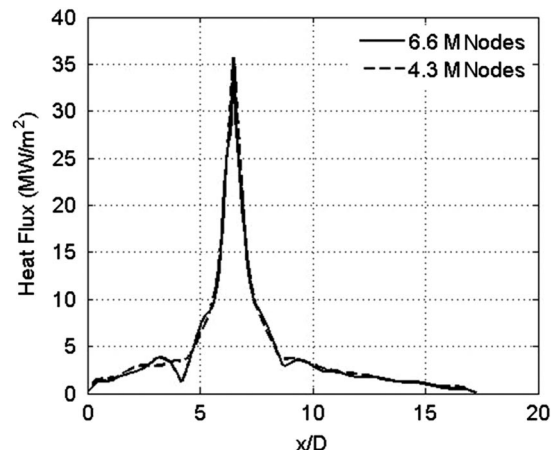Fig. 2   Schematic of the computational domain.

Fig. 4   Convective heat flux comparison in the jet impingement region with two different grids. (M denotes millions.)

variation of the heat flux at the jet impingement point is shown in Fig. 5. The average heat flux is about 45 MW/m². Snapshots of the Mach number distribution in the vertical plane passing through the nozzle centerline are shown in Fig. 6. The jet pressure ratio in the present case is close to one. Three shock diamonds that formed in the jet are distinctly visible in the Mach number plot. The jet does not

spread out or mix with cool ambient air before it impinges on the deflector. The instantaneous hot-gas mass fraction distributions in the vertical plane passing through the nozzle centerline and on the deflector surface are shown in Figs. 7a and 7b, respectively. Very little diffusion of the hot exhaust away from the jet is observed in the figure. The computed cold-wall heat flux distribution on the deflector surface is shown in Fig. 8. The peak heat flux on the order of 45 MW/m² is obtained at the jet impingement point. The computed circular pattern of the heat flux matches closely with the experimental erosion pattern (Fig. 9) on the deflector, indicating that the cold-wall heat flux is a reasonable estimate of the actual heat flux. The measured erosion depth at the jet impingement point is 14 mm.
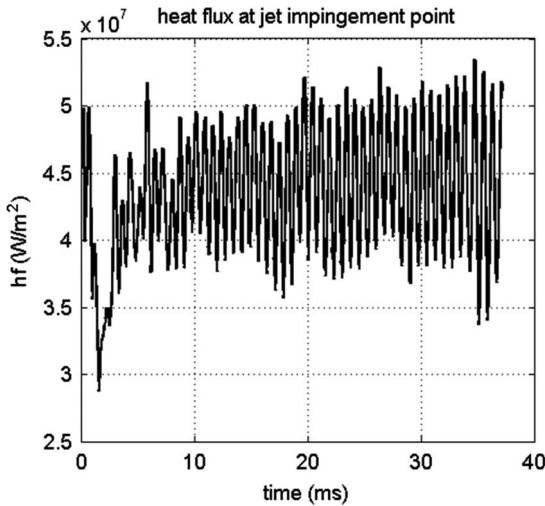

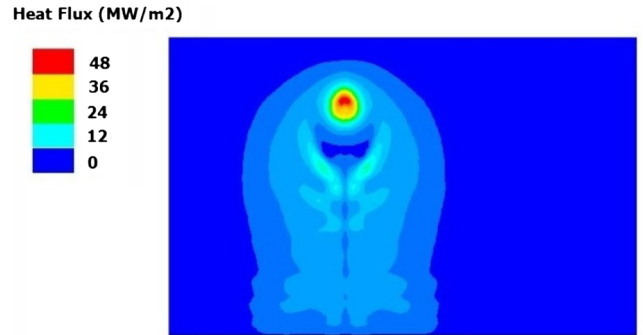Fig. 5   Heat flux variation at jet impingement point.

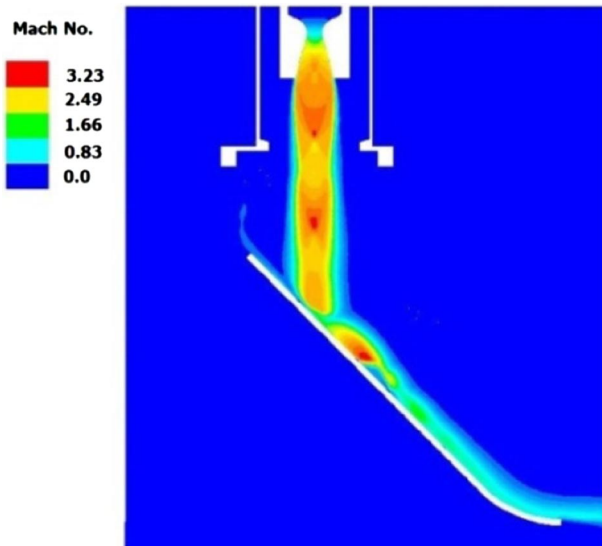Fig. 8   Computed heat flux distribution on the jet deflector surface.

Fig. 6   Instantaneous Mach number distribution in vertical plane passing through the nozzle centerline.
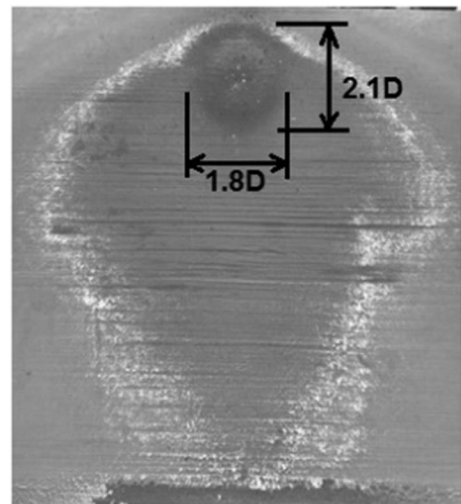

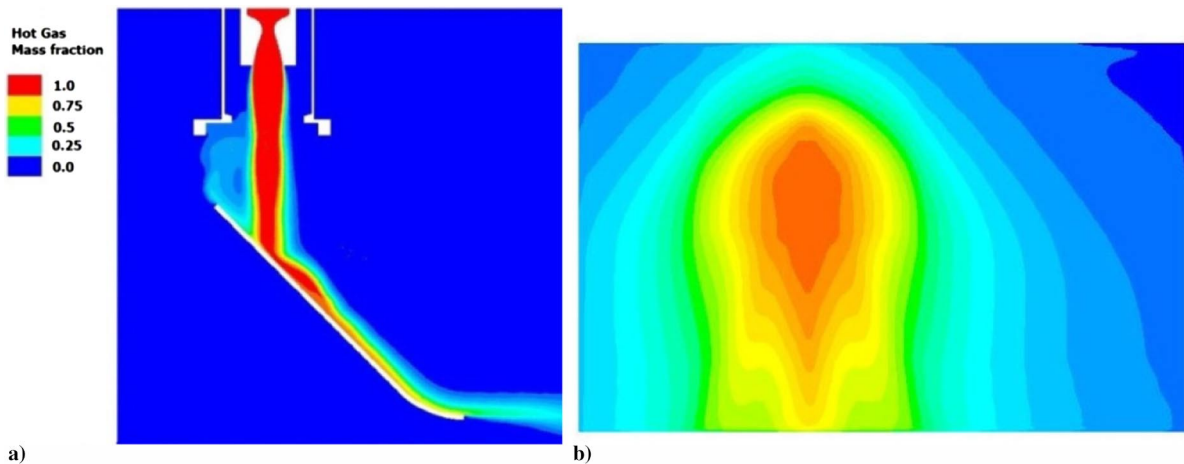Fig. 9   Experimental erosion pattern for short-burn rocket motor.

Fig. 7   Hot-gas mass fraction distribution a) in the vertical plane passing through the nozzle centerline and b) the jet deflector surface.

Erosion is moderate. Nearly half the virgin liner in the plume impingement zone is eroded.

III. Full Burn Rocket Motor Simulation with Jet Vane Thrust Vector Control

Unsteady CFD simulations were carried for the actual motor configuration to estimate the cold-wall heat flux on the deflector surface. The motor stagnation pressure and temperature were 100 bar and 2908 K, respectively. The missile had four jet vanes at the neutral position (position at which jet vanes do not generate side force). Mach number distributions in the plane passing between jet vanes (plane 1) and in the plane of jet vanes (plane 2) are shown in Figs. 10a and 10b, respectively. Due to the presence of jet vanes, and with a higher mass flow rate, the flow pattern for this case is different from the short-burn motor case without jet vanes. Also, the jet pressure ratio (exit pressure/ambient pressure) for the present case is 2.7, as compared to the value of 1.0 for the short-burn rocket case. The underexpanded jet, after coming out of the nozzle, spreads more through the gap between the brackets of the jet vanes than in the plane of the jet vanes. The hot plume can be seen affecting the side motion arrester. Figures 11a–11c depict the distribution of hot gas in plane 1, plane 2, and the jet deflector surface, respectively. Compared with the corresponding plot for the short-burn motor test (Fig. 7), it can be seen that the jet spreads wider for the motor with the jet vane TVC. Spreading of plume through the gap between the jet vane brackets gives the plume a plus-sign (+) shape. Chordwise and spanwise distributions of surface pressures in the deflector plate are shown in

Figs. 12a and 12b, respectively. Surface pressures and distances are nondimensionalized with the ambient pressure p_∞ and nozzle diameter D, respectively. The larger spread of the exhaust plume due to the presence of the jet vane in the full-burn rocket motor is clearly visible in the figure. Although the chamber pressure of the full-burn rocket motor is higher than the short-burn rocket motor, more plume spreading in the former causes a lesser peak convective heat flux. The heat flux distribution on the deflector surface is shown in Fig. 13. Although the flow rate of the missile motor is much higher than the flow rate of the short-burn motor, the heat flux at the impingement point is lower than that for the short-burn motor (Fig. 8) due to spreading of the plume from the underexpanded nozzle and in the presence of jet vanes. The heat flux pattern obtained from the CFD solution was also plus-sign shaped, but it was more prominent vertically than in the horizontal direction. Chordwise and spanwise distributions of convective heat fluxes in the deflector plate are shown in Figs. 14a and 14b, respectively. The heat flux values are nondimensionalized with the maximum heat flux of the short-burn rocket motor. Although the peak heat flux of the full-burn rocket motor $(37\ \text{MW/m}^2)$ is less when compared to the value $(45\ \text{MW/m}^2)$ for the short-burn rocket motor, the heat flux distribution pattern for the former is wider than the latter. The photograph of the jet deflector liner after the test is shown in Fig. 15. A close resemblance of the computed heat flux and the erosion pattern is observed. The measured erosion of the full-burn motor test was 26 mm, as compared to the 14 mm erosion depth of short burn. The convective heat flux of eight neighboring points (NW (North West), N (North), NE (North East), E (East), SE (South East), S
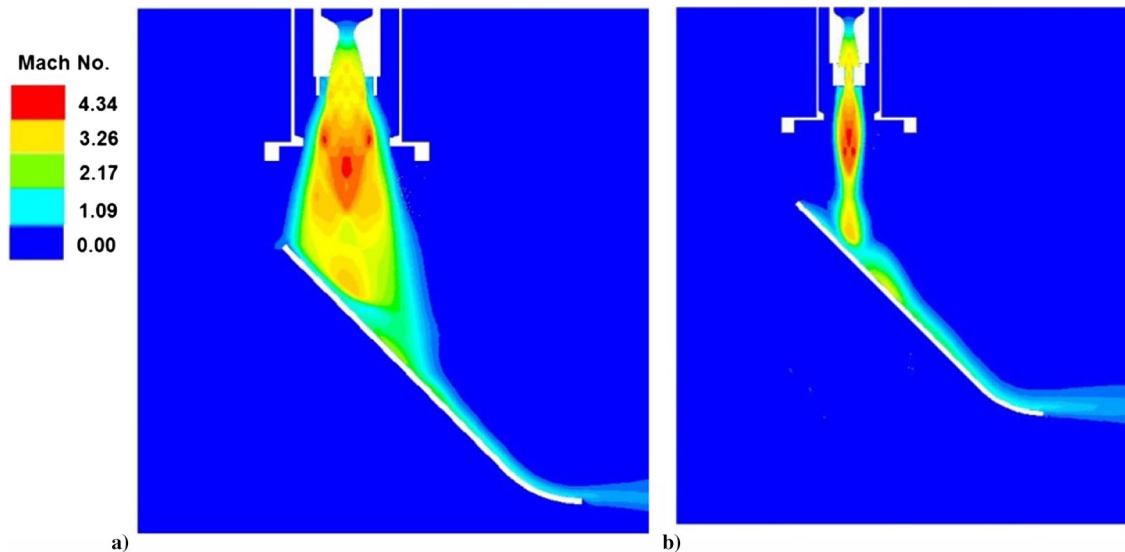

Fig. 10   Mach number distributions in plane a) passing between jet vanes (plane 1) and b) plane of jet vanes (plane 2).
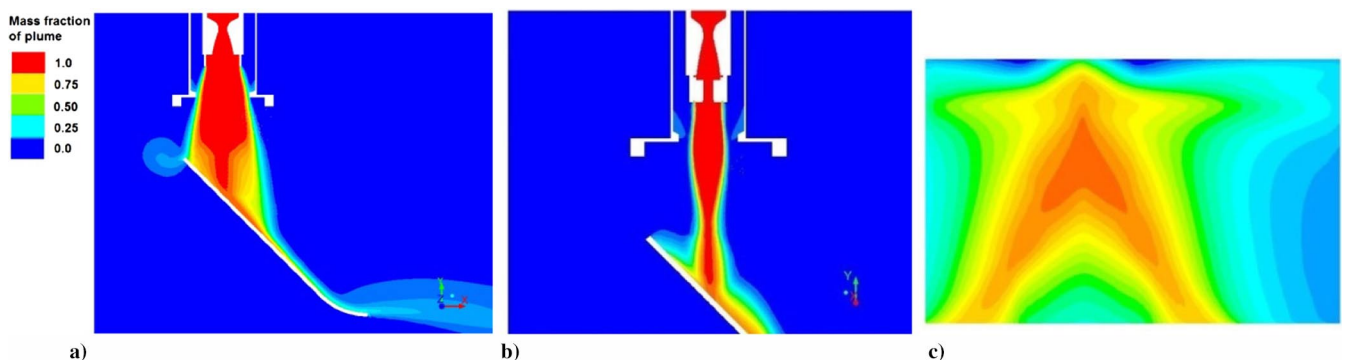

Fig. 11   Hot-gas mass fraction distributions in plane a) passing between jet vanes (plane 1) and b) plane of jet vanes (plane 2), as well as c) jet deflector surface.
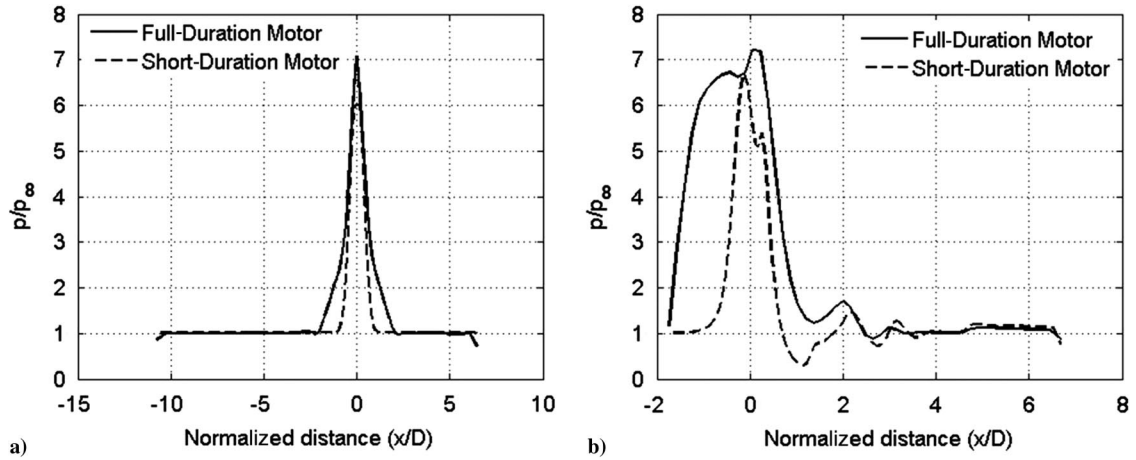
Fig. 12   Surface pressure distributions in deflector plate: a) chordwise and b) spanwise.

(South), SW (South West), and W (West)) of the maximum heat flux location C are estimated and presented in Fig. 16. The results are seen to correlate linearly with the measured erosion rate, with some scatter.

IV.   Relation Between Erosion Rate and Cold-Wall Heat Flux

The measured erosion of the short-burn motor test for a duration of 4.5 s was 14 mm, giving an average erosion rate of 3.11 (14/4.5) mm/s. The computed peak heat flux at the jet impingement point was 45 MW/m^2. So, the erosion rate per megawatt per squared meter of heat flux was 3.11/45 or 0.07 mm/s per megawatt per squared meter. For the full-duration motor test of 8.8 s, the erosion at the jet

impingement point was measured to be 26 mm, and the computed cold-wall heat flux was 37.5 MW/m^2. Hence, for this case, the erosion rate per megawatt per squared meter of heat flux was $(26/8.8)/37.5 \sim 0.078$ mm/s per megawatt per squared meter. This is close to the value obtained in the short-burn motor. The difference could be due to different thermodynamic properties of the motor gases
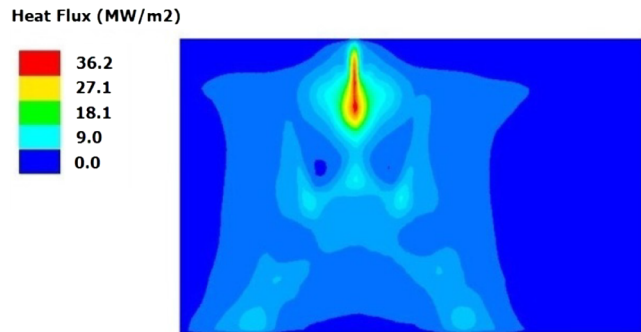

Fig. 13   Computed cold-wall heat flux on jet deflector surface.
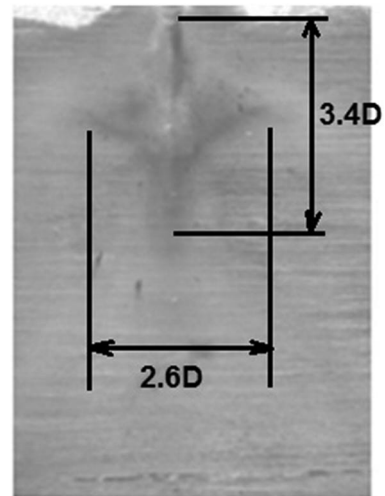

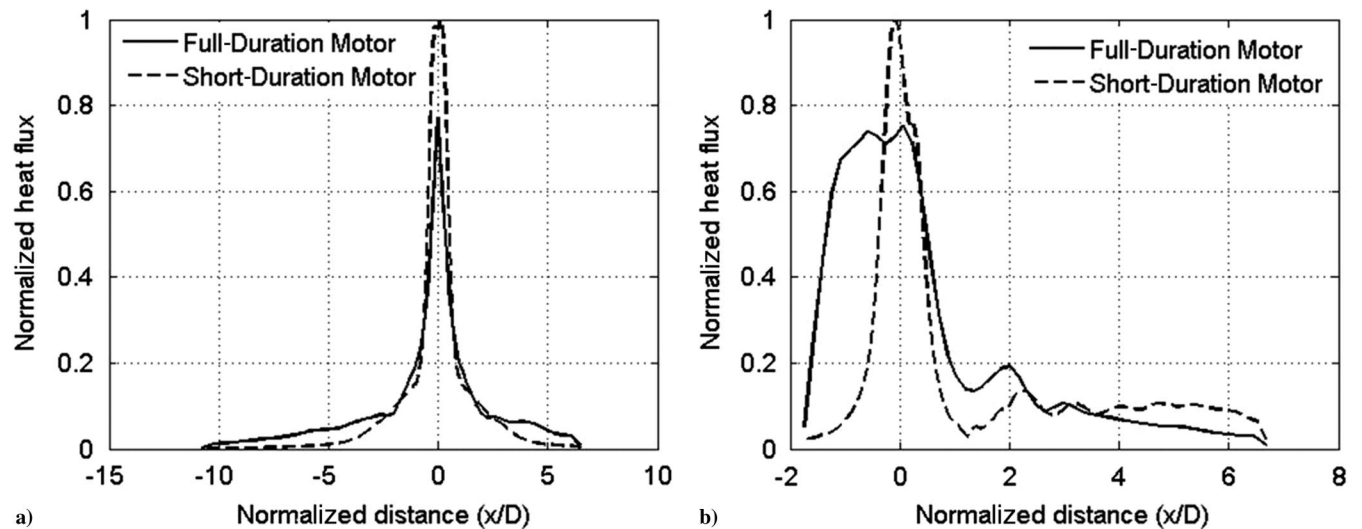Fig. 15   Photograph showing the erosion pattern on the jet deflector after the test.

Fig. 14   Convective heat flux distributions in the deflector plate: a) chordwise and b) spanwise.
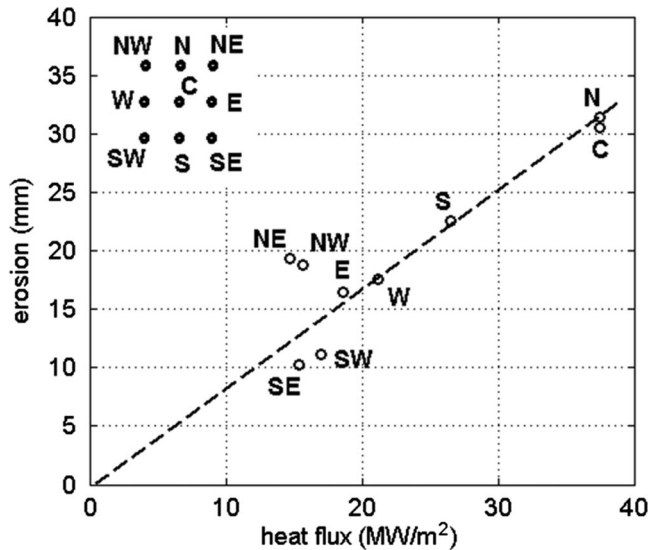
Fig. 16   Correlation of liner erosion with convective heat flux in the jet deflector.

and different flow patterns. It is conjectured that the erosion rate of the ablative liner, despite having the complex phenomenon involved, depends mainly on the heat flux on the ablative liner during jet impingement. Ablation of the same material for any other application can be estimated from these data by first estimating the cold-wall heat flux and then correlating to the ablation rate found from these data.

V.   Conclusions

Numerical simulations are carried out to estimate the cold-wall heat flux on the deflector surface due to plume impingement for a short-burn motor as well as a full-burn rocket motor with a jet vane. Three-dimensional unsteady Reynolds-averaged Navier–Stokes equations are solved along with the shear-stress transport k–ω turbulence model. The presence of jet vanes makes the exhaust plume pattern of the full-burn rocket motor considerably different than that of the short-burn rocket motor. The jet impingement zone of the full-burn rocket motor is much wider when compared to the short-burn rocket motor. The computed heat flux for the short-burn rocket motor ($45\ \mathrm{MW/m^2}$) is more than the long-duration rocket motor ($37\ \mathrm{MW/m^2}$), in spite of having a lower mass flow rate. The observed erosion patterns of both rocket motor liners are found to scale with the computed heat flux rate. The erosion rate per megawatt per squared meter of heat flux of the full-duration rocket motor is found to be 0.078 mm/s per megawatt per squared meter, as compared to the value of 0.07 mm/s per megawatt per squared meter for the short-burn rocket motor. It is conjectured that the erosion rate of the ablative liner depends mainly on the heat flux due to jet impingement.

References

[1] Ginzburg, I. P., Semilentenco, B. G., Terpigorer, V. S., and Uskov, V. N., "Some Singularities of Supersonic Underexpanded Jet Interaction with a Plane Obstacle," *Journal of Engineering Physics*, Vol. 19, No. 3, 1970, pp. 1081–1084.
doi:10.1007/BF00826231

[2] Kalghatgi, G. T., and Hunt, B. L., "Experiments on the Impingement of a Supersonic Jet on a Flat Plate," *Aeronautical Quarterly*, Vol. 27, No. 3, 1976, pp. 169–185.
doi:10.1017/S0001925900007678

[3] Lamont, P. J., and Hunt, B. L., "The Impingement of Underexpanded, Axisymmetric Jets on Perpendicular and Inclined Flat Plates," *Journal of Fluid Mechanics*, Vol. 100, No. 3, 1980, pp. 471–511.
doi:10.1017/S0022112080001255

[4] Nakai, Y., Fujimatsu, N., and Fujii, K., "Flow Classification of the Under-Expanded Super Sonic Jet Impinging on a Flat Plate," AIAA Paper 2003-3467, 2003.

[5] Nakai, Y., Fujimatsu, N., and Fujii, K., "Experimental Study of Underexpanded Supersonic Jet Impingement on an Inclined Flat Plate," *AIAA Journal*, Vol. 44, No. 11, 2006, pp. 2691–2699.
doi:10.2514/1.17514

[6] Edney, B. E., "Effects of Shock Impingement on the Heat Transfer Around Blunt Bodies," *AIAA Journal*, Vol. 6, No. 1, 1968, pp. 15–21.
doi:10.2514/3.4435

[7] Mayer, E., and Prickettt, R., "Rocket Plume Impingement Heat Transfer on Plane Surfaces," *Journal of Spacecraft and Rockets*, Vol. 24, No. 4, July–Aug. 1987, pp. 291–295.
doi:10.2514/3.25915

[8] Lengrand, J. C., Allegre, J., and Raffin, M., "Heat Transfer to a Surface Impinged Upon by a Simulated Rocket Exhaust Plume," *Progress in Astronautics and Aeronautics: Proceedings of the 12th Rarefied Gas Dynamics Symposium*, Vol. 74, Pt. 2, edited by S. S. Fisher, AIAA, New York, 1981, p. 980.

[9] McIlroy, K., and Fujii, K., "Computational Analysis of Supersonic Underexpanded Jets Impinging on an Inclined Flat Plate," AIAA Paper 2007-3859, 2007.

[10] Dharavath, M., and Chakraborty, D., "Numerical Simulation of Supersonic Jet Impingement on Inclined Plate," *Defense Science Journal*, Vol. 63, No. 4, July 2013, pp. 355–362.
doi:10.14429/dsj

[11] Yoshinori, G., Nonomura, T., and Kansai, M., "Detailed Analysis of Flat Plate Pressure Peaks Created by Supersonic Jet Impingements," AIAA Paper 2009-1289, 2009.

[12] Deng, X. G., and Zhang, H., "Developing High-Order Weighted Compact Nonlinear Schemes," *Journal of Computational Physics*, Vol. 165, No. 1, 2000, pp. 22–44.
doi:10.1006/jcph.2000.6594

[13] McManus, H. L. N., and Springer, G. S., "High Temperature Thermomechanical Behavior of Carbon-Phenolic and Carbon-Carbon Composites, I. Analysis," *Journal of Composite Materials*, Vol. 26, No. 2, 1992, pp. 206–229.
doi:10.1177/002199839202600204

[14] Henderson, J. B., and Wieck, E., "A Mathematical Model to Predict the Thermal Response of Decomposing Expanding Composite," *Journal of Composite Materials*, Vol. 21, No. 4, 1987, pp. 373–393.
doi:10.1177/002199838702100406

[15] Matting, F. W., "Analysis of Charring Ablation with Description of Associated Computing Program," NASA TN D-6085, 1970.

[16] Moyer, C. B., and Rindal, R. A., "An Analysis of the Coupled Chemically Reacting Boundary Layer and Charring Ablator—Part II—Finite Difference Solution for the In-Depth Response of Charring Materials Considering Surface Chemical and Energy Balance," NASA CR-1061, 1968.

[17] Ogasawara, T., Ishikawa, T., Yamada, T., Yokata, R., Itoh, M., and Nogi, S., "Thermal Response and Ablation Characteristics of Carbon Fiber Reinforced Composite with Novel Silicon Containing Polymer MSP," *Journal of Composite Materials*, Vol. 36, No. 2, 2002, pp. 143–157.

[18] Siddiqui, A. O., and Balasubrahmanyam, G., "Design of Ablative Liners for High Heat and Erosive Conditions," *Journal of Reinforced Plastics and Composites*, Vol. 24, No. 9, 2005, pp. 993–1007.
doi:10.1177/0731684405048202

[19] Bianchi, D., Nasuti, F., Onofri, M., and Martell, E., "Thermochemical Erosion Analysis for Graphite/Carbon–Carbon Rocket Nozzles," *Journal of Propulsion and Power*, Vol. 27, No. 1, Jan.–Feb. 2011, pp. 197–205.
doi:10.2514/1.47754

[20] *ANSYS FLUENT User Guide, Release 14.0*, ANSYS, Inc., Canonsburg, PA, Nov. 2011.

[21] ICEMCFD 14.0 Documentation, ANSYS, Inc., Canonsburg, PA, Nov. 2011.

[22] Roe, P. L., "Characteristic Based Schemes for the Euler Equations," *Annual Review of Fluid Mechanics*, Vol. 18, No. 1, 1986, pp. 337–365.
doi:10.1146/annurev.fl.18.010186.002005

S. Silton
Associate Editor